JOURNAL OF
SYNCHROTRON
RADIATION

ISSN 1600-5775

MISTRAL: a transmission soft X-ray microscopy beamline for cryo nano-tomography of biological samples and magnetic domains imaging

Andrea Sorrentino,[a] Josep Nicolás,[a] Ricardo Valcárcel,[a] Francisco Javier Chichón,[b] Marc Rosanes,[a] Jose Avila,[a] Andrei Tkachuk,[c] Jeff Irwin,[c] Salvador Ferrer[a] and Eva Pereiro[a]*

[a]ALBA Synchrotron Light Source, Cerdanyola del Vallès, Barcelona 08290, Spain, [b]Centro Nacional de Biotecnología – CSIC, Campus Cantoblanco, Madrid 28049, Spain, and [c]Zeiss, Pleasanton, CA 94588, USA. *Correspondence e-mail: epereiro@cells.es

Received 27 February 2015
Accepted 3 May 2015

Edited by J. F. van der Veen

Keywords: X-ray microscopy; tomography; correlative imaging; magnetic domains imaging.

The performance of MISTRAL is reported, the soft X-ray transmission microscopy beamline at the ALBA light source (Barcelona, Spain) which is primarily dedicated to cryo soft X-ray tomography (cryo-SXT) for three-dimensional visualization of whole unstained cells at spatial resolutions down to 30 nm (half pitch). Short acquisition times allowing for high-throughput and correlative microscopy studies have promoted cryo-SXT as an emerging cellular imaging tool for structural cell biologists bridging the gap between optical and electron microscopy. In addition, the beamline offers the possibility of imaging magnetic domains in thin magnetic films that are illustrated here with an example.

1. Introduction

In structural cell biology, microscopy is of fundamental importance to visualize and understand the organization of cellular structures and its reorganization during cellular processes. In recent years, the need to image the detailed relationship between structure and function, at various levels of resolution and length scales, has pushed towards the development of correlative imaging studies involving three-dimensional (3D) microscopic techniques: the well established visible-light and electron microscopies and the more recent soft X-ray transmission microscopy.

Visible-light microscopy can visualize *in vivo* samples but sub-cellular nanometric resolution can be achieved only by the use of fluorescent markers whereas the majority of the cellular structure remains invisible (Huang, 2010; Patterson, 2009). On the other hand, transmission electron microscopy can image complex cellular structures with a resolution of a few nanometers (Grünewald & Cyrklaff, 2006) but the low penetration power of electrons in biological materials (≤ 500 nm) makes the visualization of a whole thick eukaryotic cellular volume exceedingly time-consuming as multiple serial sections would be required (Noske *et al.*, 2008).

In this scenario, soft X-rays are a versatile probe to study biological samples due to their specific interaction with matter in the so-called water window energy range (284–543 eV), *i.e.* between the carbon and the oxygen K absorption edges (Wolter, 1952). This is due to (i) a high intrinsic penetration depth in water (up to ~ 10 μm) and (ii) a high natural contrast between water and carbon-based cellular ultrastructures. Synchrotron-based cryo-SXT has already demonstrated its ability to image the whole frozen-hydrated cell structure in 3D

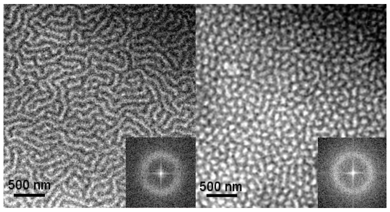

at medium resolution (30 nm half pitch resolution) bridging the gap in terms of resolution and penetration depth between fluorescence light microscopy and cryo-electron tomography (Weiss *et al.*, 2000; Schneider *et al.*, 2002, 2010; Larabell & Gros, 2004; Uchida *et al.*, 2009; Carrascosa *et al.*, 2009; Chichón *et al.*, 2012; Kapishnikov *et al.*, 2012).

MISTRAL, the soft X-ray transmission microscopy beamline dedicated to cryo-SXT at the ALBA light source, started user operation in February 2013. We report here a brief description of the beamline optics and the end-station, as well as its performance in terms of photon flux. Two scientific applications are also presented: an example of correlative microscopy investigation on frozen hydrated cells and an example of magnetic domains imaging.

2. MISTRAL optics and end-station description

Fig. 1 shows the side view of the windowless optical layout of MISTRAL (Pereiro *et al.*, 2009). The beamline was designed to provide uniform and energy-independent full illumination of the ellipsoidal glass capillary condenser (CC) for the whole energy range (270–2600 eV) with maximum photon flux. With this aim, the bending-magnet X-ray beam is focused by a Kirkpatrick–Baez mirror pair, vertically at the entrance slit (ES) and horizontally at the exit slit (XS). Between the two slits there is a vertically plane-grating monochromator (PGM), similar to Petersen's design (Petersen *et al.*, 1982), but equipped with variable-line-spacing gratings, which preserves the focusing at the exit slit, for any value of the fixed-focus constant $c_{\rm ff}$ (the ratio between the cosine of the diffracted angle and the cosine of the incident angle with respect to the normal of the grating surface). The value of $c_{\rm ff}$ can be adjusted in order to optimize flux, spectral resolution and harmonic rejection depending on the experimental requirements (Pereiro *et al.*, 2009; Howells & Staub, 1996). The monochromator system is made up by a plane mirror (PM) and two variable-line-spacing plane gratings (VLSGs), a Ni-coated grating for the low-energy range (LE: 270–850 eV) and a Pt-coated grating for the high-energy range (HE: 850–2600 eV). An elliptical mirror (VRFM) downstream of the PGM refocuses the beam vertically onto the XS. All the beamline mirrors have Ni and Rh coatings which allow good reflection efficiency in the LE and HE ranges, respectively. The measured specular beam ($c_{\rm ff}$ = 1) at full width at half-maximum on the XS plane is 28 µm (V) and 75 µm (H), in good agreement with the expected values from the optical design. Further details on the alignment strategy and mirrors optimization are given by Sorrentino *et al.* (2013). The TXM is working for the moment in the LE range. An update to the HE range is planned in the future.

The full-field transmission X-ray microscope (TXM) is mainly dedicated to cryo-SXT and was built by Xradia Inc. (now Zeiss). The TXM is contained in a high-vacuum chamber pumped with a 700 l s^{-1} turbomolecular pump. Typical working values of the pressure are in the range of low 10^{-7} mbar at cryo temperatures. The condenser (CC) is an elliptical hollow borosilicate glass capillary (Zeng *et al.*, 2008) of 100 mm length with inner entrance and exit diameters of 1.8 mm and 0.58 mm, respectively. This condenser works as a single reflection achromatic lens with a working distance of 10.05 mm. It delivers a demagnified image of the XS with a typical dimension of 2 µm^2 onto the sample. To achieve the desired field of view on the sample, the condenser is mounted on a XY piezo scanner that allows varying the amplitude and the frequency for adjusting the exposure time (usually 0.5 s or 1 s). The field of view is typically between 10 µm × 10 µm and 16 µm × 16 µm.

An objective Fresnel zone plate (OZP) lens is used after the sample to form an image of the field of view on the detector. Two Ni OZP lenses made by Zeiss with 40 nm and 25 nm outermost zone widths and 937 and 1500 zones, respectively, are available, giving focal lengths of 2.52 mm and 1.57 mm, respectively, at 520 eV. These focal lengths allow for ±70° and ±65° rotation, respectively.

A Siemens star pattern with 30 nm smallest features has been successfully imaged with both zone plate lenses (not reported here), and a method to extract the apparent transfer function of the microscope system from these images was published by Otón *et al.* (2015).

The back-illuminated CCD detector (Pixis XO by Princeton Instruments), with 1024 × 1024 pixels and 13 µm pixel size, can be moved along the optical axis (z-axis) to change the magnification from 1.5 m to 3 m from the sample position. Typical working values of the magnification are in the range 800−1600, corresponding to effective pixel sizes of 16–8 nm. Given that the primary energy of interest for SXT of vitrified samples is just below the oxygen K absorption edge, the capillary condenser has been designed to match the numerical aperture of the 40 nm OZP at 520 eV as this is the most used lens for cells imaging because it provides a larger depth of focus compared with the one given by the 25 nm OZP.

The sample holders are mounted on an XYZ stage with a repeatability of ±100 nm and ranges of ±5, ±3,

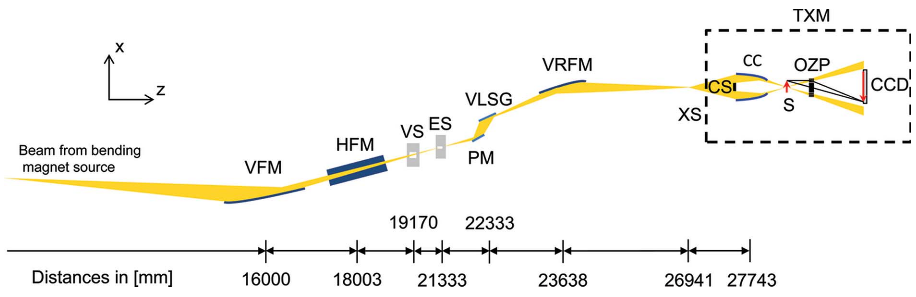

Figure 1
Scheme showing the side view of the MISTRAL beamline with the distances (not to scale) of the various optical elements from the bending-magnet source up to the vacuum chamber of the transmission X-ray microscope (TXM) (dashed rectangle) containing the central stop (CS), the capillary condenser (CC), the sample (S), the objective zone plate lens (OZP) and the CCD.

Table 1
Beamline parameters.

Source	Bending magnet
Monochromator	Variable-line-spacing plane grating
Energy resolution (theoretical)	Up to 5 × 10^3 ($E/\Delta E$)
Beamline optics energy range	270–2600 eV
TXM energy range	270–1000 eV
Flux on the sample at 520 eV	2.2 × 10^{10} photons s^{-1}
Sample format	TEM round grid (3.05 mm diameter)
Zone plates available	25 nm and 40 nm
Cryo tomography	Sample environment temperature $\simeq$ 105 K
Tilt range	±65° (25 nm ZP); ±70° (40 nm ZP)
Detector	PIXIS X0: 1k × 1k pixels, pixel size 13 µm

±5 mm, respectively. The translation stage is mounted on top of a rotation table with a run-out below 0.5 µm. The practical angular rotation range at 520 eV is ±70° due to the geometrical limitation imposed by the use of a flat sample and the OZP focal length. At lower energies, the rotation range has to be reduced accordingly to the OZP focal length. This limited tilting range results in a region empty of information in the Fourier space, the so-called 'missing wedge', which in real space produces an elongation of every point of the reconstructed volume along the beam direction (as in electron tomography). In addition to this effect, there is an added blurring which is more important than that related to the missing wedge. It occurs again along the beam direction, when the specimen is thicker than the depth of field of the lens (Weiss *et al.*, 2000; Attwood, 1999; Howells *et al.*, 2007; Bertilson *et al.*, 2011; Otón *et al.*, 2012), which in practice is often the case in the water window energy range.

For biological applications, cryogenic environment is required to reduce radiation damage and avoid mass loss during data collection. The control and sample handling under cryogenic conditions necessary to preserve the vitrified state of the frozen hydrated samples, which requires $T < 138$ K (Dubochet *et al.*, 1988), is accomplished with a cryo system developed by Zeiss and described recently by Chen *et al.* (2014). The TXM has the capability to image standard electron microscopy grids (of 3 mm diameter) for biological applications, which are convenient for growing flat adherent cells such as mammalian cell monolayer cultures. However, the sample stage set-up allows for tailored sample holder designs that might be required for other applications such as, for instance, the imaging of magnetic domains (see example below).

Some of the beamline parameters discussed here have been summarized in Table 1.

3. Flux measurements

Fig. 2(*a*) reports the measured flux as a function of energy at the exit slit plane (red curve) and at the sample position (black curve) for the LE range when normalized to 100 mA storage ring electron current and with a $c_{\rm ff}$ of 2.25 (Pereiro *et al.*, 2009). For tomography, a $c_{\rm ff}$ of 2.25 provides a good compromise between flux and resolving power. For these measurements, a photodiode was installed at the XS and in the divergent beam just after the sample position at which a 20 µm pinhole was located. The photodiode current values were calibrated with respect to the efficiency curves provided by the manufacturer. Being the flux collected from the bending-magnet source in the LE range of the order of 10^{12} photons s^{-1} (0.1% bandwidth)$^{-1}$, and accounting for 90% reflectivity of the mirrors and 15% efficiency of the Ni VLSG, our flux measurement at the XS is in good agreement with the expected one of about 10^{11} photons s^{-1} (0.1% bandwidth)$^{-1}$ (red curve in Fig. 2*a*). Several features are clearly visible in the plots of Fig. 2(*a*): (i) a maximum around 740 eV which corresponds to the theoretical maximum efficiency of the Ni VLSG, (ii) a minimum around the C *K*-edge (284 eV) arising from the beamline optics contamination and the lower grating efficiency at that energy, (iii) the presence of nitrogen (410 eV), (iv) the drop at the oxygen *K*-edge (543 eV) due to the optics contamination (red curve) and to the absorption of the borosilicate capillary condenser (black curve) and (v) the absorption of the Ni optics coating at the Ni L_3-edge (852 eV). We have estimated the CC efficiency shown in Fig. 2(*b*) for energies above 425 eV only, as for lower energies and with a $c_{\rm ff}$

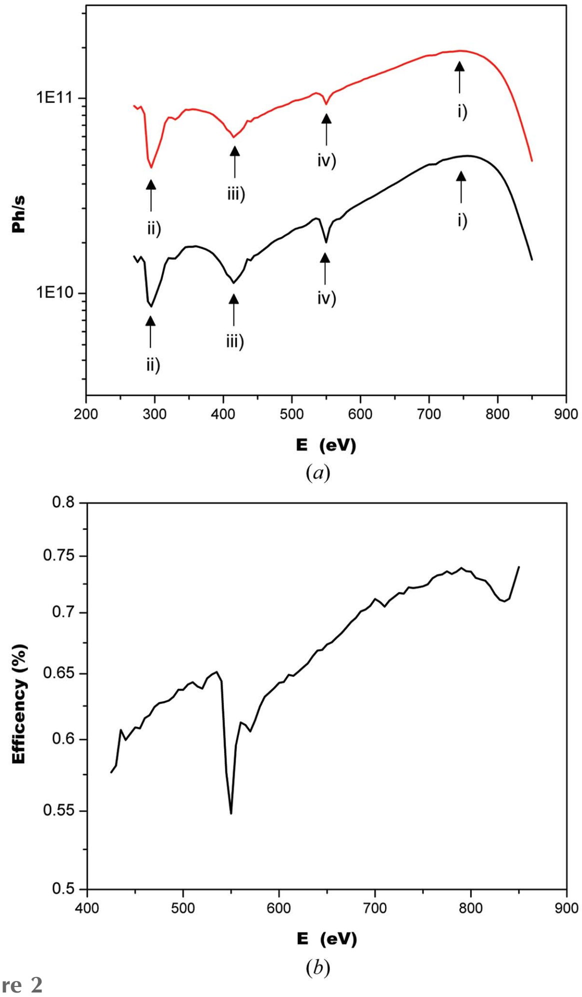

(*a*)

(*b*)

Figure 2
(*a*) Photon flux at the XS plane (red line) and impinging flux on the sample (black line) as a function of the energy for the LE range. The arrows indicate the main features of the two plots as described in the text. (*b*) Estimated capillary condenser efficiency from the measurements shown in (*a*).

of 2.25 the second diffraction order of the grating reaches the XS. Higher harmonic rejection is achieved by decreasing the $c_{\rm ff}$ but this implies decreasing as well the resolving power. As shown, an overall increase of the efficiency with increasing energy is revealed, going from 60% to 75% except for the drop at the oxygen K-edge corresponding to the absorption of the borosilicate glass capillary condenser (as mentioned above). At 520 eV the CC efficiency is of about 65%. The flux at the sample allows the collection of tomograms in 5–15 min depending on the sample and its vitreous ice thickness.

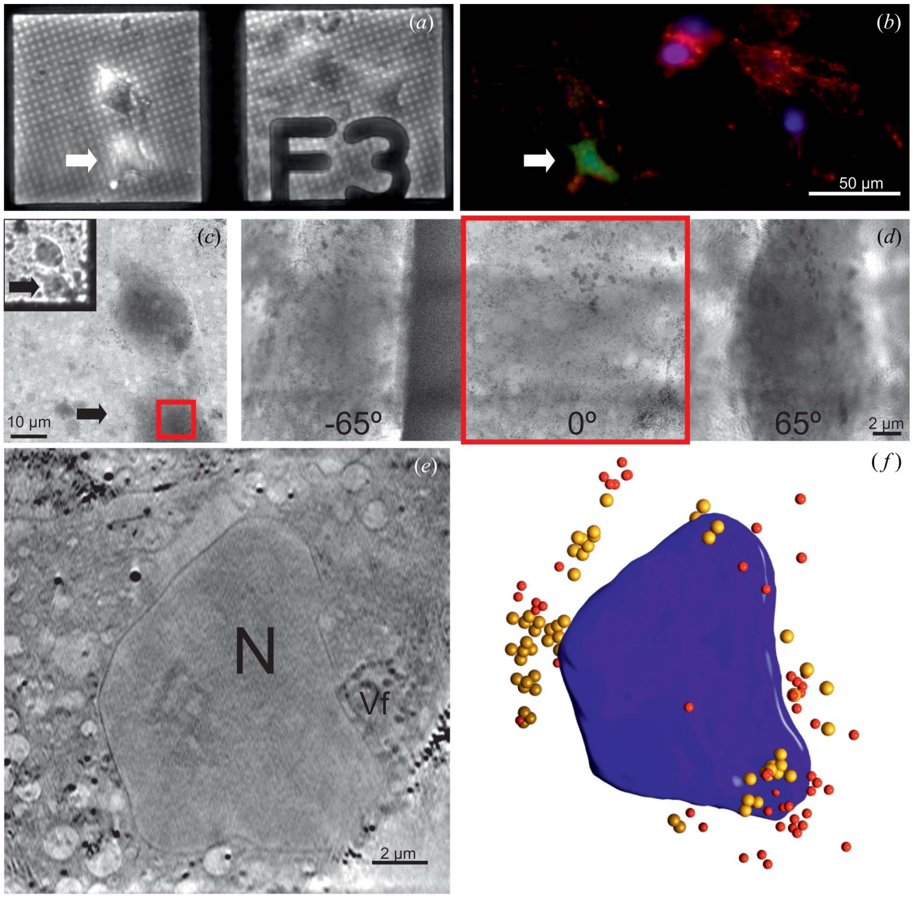

Figure 3
Correlative microscopy of PtK2 infected cells with vaccinia virus. *In vivo* light microscopy (*a*) and epifluorescence images (*b*) of the cells growing on a holey carbon grid. In (*b*), DAPI (in blue) labels the DNA, WGA (in red) labels membranes of the cell and GFP (in green) is expressed only by the infected cells. (*c*) 2D X-ray mosaic composition (images stitching) of the same area of the grid shown in (*a*) and (*b*). The inset shows a cryo bright-field light microscopy image with the on-line light microscope of the TXM in which the two cells of (*a*) and (*b*) are clearly visible. The arrows from (*a*) to (*c*) point to the position of the same infected cell. (*d*) −65°, 0° and 65° TXM projection images of the selected cell at higher magnification. (*e*) Virtual slice of the reconstructed soft X-ray cryo-tomogram in the *xy* plane. N marks the position of the cell nucleus. (*f*) Segmented volume in the *xy* plane of the 3D tomographic reconstruction. The nucleus in blue is surrounded by two different viral forms, mature and immature, inside the cell in red and yellow, respectively.

4. Scientific applications

4.1. Correlative imaging of cells

Until now, cryo-SXT has been used for imaging a variety of biological samples, ranging from isolated vaccinia virus (Carrascosa *et al.*, 2009), to yeasts and protozoa (Parkinson *et al.*, 2008; Uchida *et al.*, 2009; Hummel *et al.*, 2012), to finally mammalian cells (Hanssen *et al.*, 2011, 2012; Kapishnikov *et al.*, 2012; Chichón *et al.*, 2012; Hagen *et al.*, 2012, 2014; Clowney *et al.*, 2012; Duke *et al.*, 2014; Cruz-Adalia *et al.*, 2014). It has proven to be a useful imaging tool for investigating pathogen–host interaction, cellular contacts, cellular organelles and nuclei.

One of the first applications carried out at MISTRAL was the investigation of the cellular rearrangement caused by the vaccinia virus infection in PtK2 cells at different post-infection times, as well as the quantification of the number of morphogenetic intermediates in the cell. Previous results were published by Chichón *et al.* (2012). This investigation was not possible using electron microscopy as thin sample sections are required and reconstructing the full cellular volume is exceedingly time-consuming and prone to artefacts. On the other hand, optical microscopy does not provide the necessary spatial resolution. We are presenting here the workflow of such an investigation which illustrates an example of correlative imaging study.

The sample preparation was carried out at the CNB-CSIC in Madrid (Spain) by the group led by Dr F. J. Chichón and Professor J. L. Carrascosa. PtK2 cells infected with GFP-expressing vaccinia virus were grown on electron microscopy grids (Chichón *et al.*, 2012). The grids were imaged by *in vivo* light microscopy (Fig. 3*a*) and epifluorescence (Fig. 3*b*) first, where nicely infected cells could be easily identified [for instance, the green cell shown in Fig. 3(*b*) indicated by the white arrow]. Then the grid was plunge-frozen and loaded into the TXM vacuum chamber, in which an on-line optical microscope with an objective 10× allows for a rough location of the same infected cell in Figs. 3(*a*) and 3(*b*) as can be seen in the inset of Fig. 3(*c*) where the same infected cell is indicated by a black arrow. The full mesh square (100 µm × 100 µm mosaic composed of 2D single images) of the selected infected cell (black arrow) is then imaged at 520 eV (Fig. 3*c*). A tomogram is collected at the desired position: the −65°, 0° and 65° projections are shown in Fig. 3(*d*) and a reconstructed slice is shown in Fig. 3(*e*). Finally, the segmentation of the viral forms (mature in red and immature virion in yellow) and the nucleus of the cell (in blue) are shown in Fig. 3(*f*).

At the beamline, a cryo stand-alone sample stage allows imaging vitrified samples both in epifluorescence and bright-field modalities before the beam time to select the biologically relevant best prepared grids after vitrification in case this cannot be done at the users' laboratories. This screening procedure of grids increases the efficiency of data collection at the beamline in two ways. First, it allows the user to create a map of the grid for an easy location of relevant cells or features within the cells when the grid will be loaded into the TXM vacuum chamber. Second, it allows discarding those grids with an inappropriate number of cells, ice thickness or carbon foil preservation. The installation of a fluorescent light microscope on-line with the TXM with a 20× objective lens is planned as an upgrade of the system at the end of 2015.

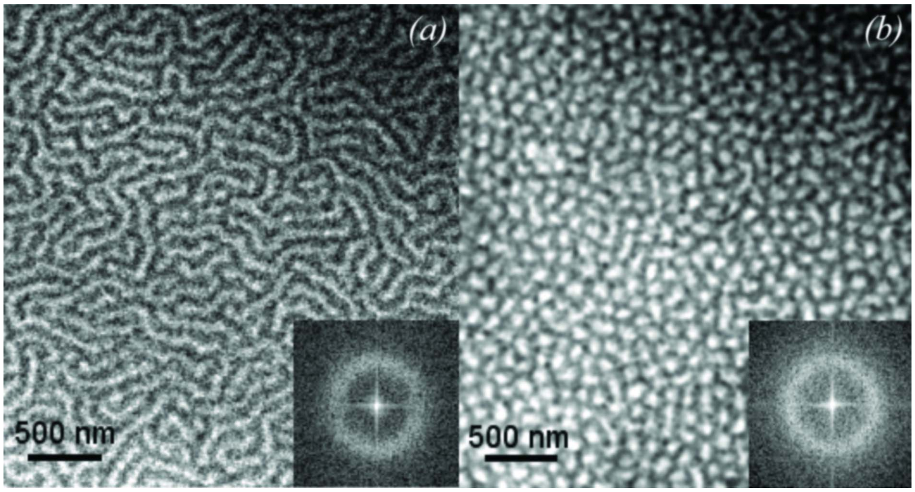

Figure 4
(*a*) Labyrinth domains and (*b*) 60 nm bubble shape domains in the same area of a 80 nm-thick $NdCo_5$ film, provided by Dr C. Quirós from Oviedo University (Spain), before and after the application of an external magnetic pulse perpendicular to the sample surface of 0.53 T (corresponding to about 70% of the saturation field) during 15 µs.

4.2. Imaging of magnetic domains

The study of the topology and structure of magnetic domains in low-dimensional systems, such as magnetic thin films and multilayered magnetic systems, is one of the active topics in both fundamental and applied studies in modern research in nanomagnetism. A thorough characterization of magnetic microstructures in such systems, occurring on short length scales in the nanometer range, provides valuable key information. The MISTRAL TXM beamline was also designed to allow the use of circularly polarized light for imaging magnetic domains using circular dichroic absorption contrast (Kang *et al.*, 2005; Fischer *et al.*, 1998). Circularly polarized X-rays can be collected by obstructing 75% of the bending-magnet beam and using the remaining 25% of the beam by selecting the lower or upper part of the reflected photons from the VFM. The beam selection is performed by a vertical slit (VS) placed just after the KB mirror pair and before the entrance slit of the monochromator (as shown in Fig. 1). Being a photon-in/photon-out technique, it allows the application to the sample of external magnetic fields and therefore the study of the microscopic changes in the structure of domains. Transmission X-ray microscopy also allows having information of buried interfaces of multi-layered films.

To investigate domain structural changes, a specific sample holder with appropriate coils allowed the generation of pulsed fields up to 1.2 T during 15 µs. After one or several pulses of different amplitudes, the samples were measured at remanence. Fig. 4(*a*) shows the characteristic labyrinth domains, which are the most common magnetic structure, after applying saturation pulses either positive or negative on a 80 nm-thick $NdCo_5$ film. The film was grown by sputtering techniques by the group of Dr C. Quirós at Oviedo University (Spain). Black and white domains correspond to inward and outward perpendicular magnetizations. The inset is the Fourier transform which shows a ring pattern indicating azimuthal disorder. The inverse of the radius of the ring gives the lateral correlation length of the distribution which is about 120 nm. Applying pulses of selected amplitudes below the saturation of the perpendicular magnetization resulted in a bubble domain structure (Fig. 4*b*) with a very narrow distribution of the dimensions of the bubbles which had a diameter of about 60 nm. The bubbles have mostly six-fold and also five-fold coordination and do not display long-range order as shown by the annular shape of the Fourier transform in the inset.

5. Summary

The MISTRAL beamline at ALBA allows for cryo soft X-ray tomography of frozen hydrated samples in the water window energy range with spatial resolution down to 30 nm half-pitch. The epifluorescence microscope future upgrade inside the vacuum chamber of the TXM will facilitate even more correlative microscopy approaches which are essential in structural cell biology. Spectroscopic 2D and 3D imaging is also possible and has been recently used by Chiappi *et al.* (CNB-CSIC) for the investigation of super-paramagnetic nanoparticles uptake by MCF-7 cells (Chiappi, 2014). Other applications such as magnetic imaging have been demonstrated. The versatility of the sample stage allows designing specific sample holders depending on the experimental requirements which opens the door to a variety of scientific cases beyond the main demanded one, cryo-SXT of cells.

Acknowledgements

We are grateful to Dr C. Quirós (Oviedo University, Oviedo, Spain) and Professor J. L. Carrascosa (CNB-CSIC, Madrid, Spain) for the samples preparation and fruitful discussions on magnetic imaging and biological applications, respectively.

References

Attwood, D. T. (1999). *Soft X-rays and Extreme Ultraviolet Radiation: Principles and Applications.* Cambridge University Press.

Bertilson, M., von Hofsten, O., Hertz, H. M. & Vogt, U. (2011). *Opt. Express*, **19**, 11578–11583.

Carrascosa, J. L., Chichón, F. J., Pereiro, E., Rodríguez, M. J., Fernández, J. J., Esteban, M., Heim, S., Guttmann, P. & Schneider, G. (2009). *J. Struct. Biol.* **168**, 234–239.

Chen, S., Deng, J., Yuan, Y., Flachenecker, C., Mak, R., Hornberger, B., Jin, Q., Shu, D., Lai, B., Maser, J., Roehrig, C., Paunesku, T., Gleber, S. C., Vine, D. J., Finney, L., VonOsinski, J., Bolbat, M., Spink, I., Chen, Z., Steele, J., Trapp, D., Irwin, J., Feser, M., Snyder, E., Brister, K., Jacobsen, C., Woloschak, G. & Vogt, S. (2014). *J. Synchrotron Rad.* **21**, 66–75.

Chiappi, M. (2014). PhD Thesis, Universidad Autónoma de Madrid, Spain.

Chichón, F. J., Rodríguez, M. J., Pereiro, E., Chiappi, M., Perdiguero, B., Guttmann, P., Werner, S., Rehbein, S., Schneider, G., Esteban, M. & Carrascosa, J. L. (2012). *J. Struct. Biol.* **177**, 202–211.

Clowney, E. J., LeGros, M. A., Mosley, C. P., Clowney, F. G., Markenskoff-Papadimitriou, E. C., Myllys, M., Barnea, G., Larabell, C. A. & Lomvardas, S. (2012). *Cell*, **151**, 724–737.

Cruz-Adalia, A., Ramirez-Santiago, G., Calabia-Linares, C., Torres-Torresano, M., Feo, L., Galán-Díez, M., Fernández-Ruiz, E., Pereiro, E., Guttmann, P., Chiappi, M., Schneider, G., Carrascosa, J. L., Chichón, F. J., Martínez Del Hoyo, G., Sánchez-Madrid, F. & Veiga, E. (2014). *Cell Host Microbe*, **15**, 611–622.

Dubochet, J., Adrian, M., Chang, J. J., Homo, J. C., Lepault, J., McDowall, A. W. & Schultz, P. (1988). *Q. Rev. Biophys.* **21**, 129–228.

Duke, E. M., Razi, M., Weston, A., Guttmann, P., Werner, S., Henzler, K., Schneider, G., Tooze, S. A. & Collinson, L. M. (2014). *Ultramicroscopy*, **143**, 77–87.

Fischer, P., Eimüller, T., Schütz, G., Guttmann, P., Schmahl, G., Pruegl, K. & Bayreuther, G. (1998). *J. Phys. D*, **31**, 649–655.

Grünewald, K. & Cyrklaff, M. (2006). *Curr. Opin. Microbiol.* **9**, 437–442.

Hagen, C., Guttmann, P., Klupp, B., Werner, S., Rehbein, S., Mettenleiter, T. C., Schneider, G. & Grünewald, K. (2012). *J. Struct. Biol.* **177**, 193–201.

Hagen, C., Werner, S., Carregal-Romero, S., Malhas, A. N., Klupp, B. G., Guttmann, P., Rehbein, S., Henzler, K., Mettenleiter, T. C., Vaux, D. J., Parak, W. J., Schneider, G. & Grünewald, K. (2014). *Ultramicroscopy*, **146**, 46–54.

Hanssen, E., Knoechel, C., Dearnley, M., Dixon, M. W., Le Gros, M., Larabell, C. & Tilley, L. (2012). *J. Struct. Biol.* **177**, 224–232.

Hanssen, E., Knoechel, C., Klonis, N., Abu-Bakar, N., Deed, S., LeGros, M., Larabell, C. & Tilley, L. (2011). *J. Struct. Biol.* **173**, 161–168.

Howells, M., Jacobsen, C. & Warwick, T. (2007). *Principles and Applications of Zone Plate X-ray Microscopes*, ch. 13, *Science of Microscopy*. New York: Springer.

Howells, M. R. & Staub, U. (1996). PSI report 96-20. Paul Scherrer Institut, Villigen, Switzerland.

Huang, B. (2010). *Curr. Opin. Chem. Biol.* **14**, 10–14.

Hummel, E., Guttmann, P., Werner, S., Tarek, B., Schneider, G., Kunz, M., Frangakis, A. S. & Westermann, B. (2012). *PLoS One*, **7**, e53293.

Kang, B. S., Fischer, P., Kim, D. H., Attwood, D., Anderson, E. & Cho, G. (2005). *IPAP Conf. Ser.* **7**, 288–290.

Kapishnikov, S., Weinera, A., Shimonib, E., Guttmann, P., Schneider, G., Dahan-Pasternakd, N., Dzikowskid, R., Leiserowitza, L. & Elbauma, M. (2012). *Proc. Natl Acad. Sci.* **109**, 11188–11193.

Larabell, C. A. & Le Gros, M. A. (2004). *Mol. Biol. Cell*, **15**, 957–962.

Noske, A. B., Costin, A. J., Morgan, G. P. & Marsh, B. J. (2008). *J. Struct. Biol.* **161**, 298–313.

Otón, J., Sorzano, C. O., Marabini, R., Pereiro, E. & Carazo, J. M. (2015). *Opt. Express*, **23**, 9567–9572.

Otón, J., Sorzano, C. O., Pereiro, E., Cuenca-Alba, J., Navarro, R., Carazo, J. M. & Marabini, R. (2012). *J. Struct. Biol.* **178**, 29–37.

Parkinson, D. Y., McDermott, G., Etkin, L. D., Le Gros, M. A. & Larabell, C. A. (2008). *J. Struct. Biol.* **162**, 380–386.

Patterson, G. H. (2009). *Semin. Cell Dev. Biol.* **20**, 886–893.

Pereiro, E., Nicolás, J., Ferrer, S. & Howells, M. R. (2009). *J. Synchrotron Rad.* **16**, 505–512.

Petersen, H., Jung, C., Hellwig, C., Peatman, W. B. & Gudat, W. (1982). *Rev. Sci. Instrum.* **66**, 1–14.

Schneider, G., Anderson, E., Vogt, S., Knöchel, C., Weiss, D., Legros, M. & Larabell, C. (2002). *Surf. Rev. Lett.* **09**, 177–183.

Schneider, G., Guttmann, P., Heim, S., Rehbein, S., Mueller, F., Nagashima, K., Heymann, J. B., Müller, W. G. & McNally, J. G. (2010). *Nat. Methods*, **7**, 985–987.

Sorrentino, A., Pereiro, E., Valcárcel, R., Ferrer, S. & Nicolás, J. (2013). *Proc. SPIE*, **8848**, 11–16.

Uchida, M., McDermott, G., Wetzler, M., Le Gros, M. A., Myllys, M., Knoechel, C., Barron, A. E. & Larabell, C. A. (2009). *Proc. Natl Acad. Sci. USA*, **106**, 19375–19380.

Weiss, D., Schneider, G., Niemann, B., Guttmann, P., Rudolph, D. & Schmahl, G. (2000). *Ultramicroscopy*, **84**, 185–197.

Wolter, H. (1952). *Ann. Phys.* **445**, 94–114.

Zeng, X., Duewer, F., Feser, M., Huang, C., Lyon, A., Tkachuk, A. & Yun, W. (2008). *Appl. Opt.* **47**, 2376–2381.